

This is an Open Access document downloaded from ORCA, Cardiff University's institutional repository: <https://orca.cardiff.ac.uk/id/eprint/142647/>

This is the author's version of a work that was submitted to / accepted for publication.

Citation for final published version:

Lu, Xiuyuan and Roldan, Alberto 2021. Are carbon-based materials good supports for the catalytic reforming of ammonia? *Journal of Physical Chemistry C* 125 (29) , pp. 15950-15958.
10.1021/acs.jpcc.1c03996

Publishers page: <http://dx.doi.org/10.1021/acs.jpcc.1c03996>

Please note:

Changes made as a result of publishing processes such as copy-editing, formatting and page numbers may not be reflected in this version. For the definitive version of this publication, please refer to the published source. You are advised to consult the publisher's version if you wish to cite this paper.

This version is being made available in accordance with publisher policies. See <http://orca.cf.ac.uk/policies.html> for usage policies. Copyright and moral rights for publications made available in ORCA are retained by the copyright holders.



Are Carbon-Based Materials Good Supports for the Catalytic Reforming of Ammonia?

Xiuyuan Lu, Alberto Roldan*

Cardiff Catalysis Institute, School of Chemistry, Cardiff University, Main Building, Park Place, Cardiff, CF10 3AT, UK

Abstract: Carbon-based materials are commonly used in catalysis as metal-free catalysts and as support for metal particles. We investigated a series of graphene point defects on the NH₃ reforming process using the density functional theory and shed light on their role in the catalytic reforming of ammonia. The adsorption of molecules and intermediates on carbon vacancies, lattice reconstructions, partial oxidations and dopants was analyzed to provide details on the most favorable interactions. Thermochemical investigations revealed the structures active for NH₃ adsorption and dehydrogenation. However, these defects are ineffective to desorb the reaction products, i.e., N₂ and H₂. Based on transition state theory, we implemented microkinetic simulations and found that the rate-determining step is either the NH₃ activation or the desorption of reformed molecules, depending on the defect type. Batch reaction simulations within a wide temperature and time range indicated that, although the NH₃ dehydrogenation may occur, the active sites become poisoned by the H or N anchored atoms; therefore, in the long term, carbon-based materials are inert towards the NH₃ reforming.

Keywords: Ammonia reforming; Graphene/Graphite; carbon materials, supported catalysts, Hydrogen; Microkinetics; Catalysis; DFT method

1. Introduction

The development of reliable and economic hydrogen energy technologies is one of the most prominent research topics in current times. The direct industrial implementation of hydrogen energy is inhibited by high risks and costs associated with its transport and storage.^{1,2} Compared with other molecular energy vectors, such as methanol, ethanol, formic acid, and methane, ammonia (NH₃) is a suitable carbon-free hydrogen energy carrier with high hydrogen capacity (17.64 wt%) and stable properties under mild conditions.³⁻⁶ Catalysts promoting the NH₃ reforming process are not trivial, and usually, the catalysts' supports play a crucial role in the reaction efficiency.⁷ Indeed, the catalyst's support should have a large area with inert or synergistic properties to the aimed reaction. Carbon-based materials have long been deemed suitable catalyst supports because of their high surface area, chemical resistance, low cost, and good recycling properties.⁸

Carbon-based supports have shown catalytic activity by themselves. Pereira and co-workers used carbon nanotubes as catalysts for the oxidative dehydrogenation of ethylbenzene to styrene with a conversion of 19.6% catalyzed by the untreated carbon material.⁹ Qu *et al.* found N-doped graphene to be a metal-free electrode with three-times higher electrocatalytic activity than platinum for the

oxygen reduction reaction (ORR).¹⁰ Furthermore, Zhang *et al.* investigated the mechanism of ORR on point defects in graphene clusters for fuel cell applications using density functional theory (DFT) methods.¹¹ Su *et al.* studied the impact of defects in graphene oxide on the catalytic activities for the oxidative coupling of amines to imines. The results suggest that the enhanced catalytic activity can be linked to the unpaired electrons in the system.¹² Although there is plenty of research focusing on applying carbon-based supports and carbon catalysts, the mechanism of NH₃ reforming on defective graphene remains unclear.^{13,14}

Point defects (including vacancies and lattice heteroatoms) are the most fundamental defects on graphene surfaces, which can be detected under advanced microscopic technologies. These point defects modify the local electronic structure and the properties of carbon-based materials.^{15–18} The literature on defective graphene suggests that single vacancies and mixed defects show a strong combination with hydrogen, providing a compelling advantage to retain it over pristine graphene.¹⁹ Therefore, these point defects have the potential to be active sites for NH₃ reforming. However, the short life span of intermediates and complex micro-structures concerning the reaction processes at the atomic level thwart the investigations of carbocatalysis on point defects.

For this reason, we performed DFT and microkinetic analyses on defective graphene to provide accurate information on their role on the NH₃ reforming process. This paper discusses the reaction pathway of NH₃ reforming on the different point defects, the results on batch and temperature-programmed desorption simulations on promising candidates. We rationalized the results observed using accurate electronic structure calculations and shed light on carbon-based materials for NH₃ reforming and H₂ storage.

2. Methodology

The Vienna Ab-initio Simulation Package (VASP) was employed to simulate the NH₃ reforming reaction on defective and doped graphene within the DFT frameworks.^{20,21} The spin-polarized revised Perdew-Burke-Ernzerhof (rPBE) method of the generalized gradient approximation (GGA) was adopted to describe the exchange-correlation with a plane-wave kinetic cutoff energy of 500 eV.²² The projector augmented wave (PAW) includes non-spherical contributions from the core to the gradient corrections.^{23–25} The long-range interactions were characterized by the DFT-D3 method of Grimme with zero dampings.²⁶ The optimized convergence thresholds of internal forces and electronic relaxation were set to 0.02 eV/Å and 10⁻⁵ eV, respectively. A 3×3×1 k-spacing Monkhorst-Pack grid sampled the Brillouin zone with a smearing broadening of 0.2 eV.

The optimized lattice parameter of pristine graphene is 2.469 Å, which is in agreement with the benchmark value, 2.460 Å.²⁷ All surfaces were represented by a supercell slab model (vacancies and Stone-Wales defects: $p(6\times6)$; doped: $p(4\times4)$) to avoid the interaction between defects. We added 15 Å of vacuum perpendicular to the slab to prevent any spurious interaction with periodic images. Dipole correction perpendicular to the surface was applied upon the molecular adsorption.

The molecular adsorption energy (E_{ads}) is defined by Equation 1, and the relative energy (ΔE) is calculated by Equation 2:

$$E_{ads} = E_{system} - E_{surface} - E_{molecule} \quad \text{Equation 1}$$

$$\Delta E = E_{system} + \frac{n}{2} * E_{H_2} - E_{surface} - E_{NH_3} \quad \text{Equation 2}$$

Where E_{system} is the total energy of the adsorbed system, $E_{surface}$ denotes the energy of the clean surface, including pristine graphene and the defects, E_{NH_3} and E_{H_2} are the energies of NH_3 and H_2 isolated molecules. The half energy of the hydrogen molecule refers to the energy of one H atom, and n is the number of H dissociated from NH_3 in the particular stage defining ΔE . The formation energy of defective graphene surfaces is represented by Equation 3.

$$E_{formation} = E_{defects} - n * E_{graphene} \quad \text{Equation 3}$$

Where $E_{defects}$ is the energy of the defective surface, n is the number of atoms in the slab, and $E_{graphene}$ is the energy of pristine graphene per atom. The energy of the transition states (TS) between intermediates along the reaction profiles was determined by the climbing image nudged elastic band (ci-NEB) combined with the improved dimer method (IDM), ensuring a unique imaginary frequency along the reaction coordinate.²⁸⁻³⁰ We defined the activation barriers (E_a) as the energy difference between the TS and the initial states (IS). The reaction energies (E_r) are given by the difference between the final states (FS) and the IS energies. A negative value indicates an exothermic reaction step (Equation 4).

$$E_a = E_{TS} - E_{IS} \quad \text{Equation 4}$$

$$E_r = E_{FS} - E_{IS} \quad \text{Equation 5}$$

We implemented the thermodynamic and kinetic outcomes obtained from DFT into NH_3 reforming microkinetic simulations grounded on the transition state theory (TST).³¹⁻³³ The thermochemistry and kinetic models are detailed in the Supporting Information (SI).

3. Results and discussion

3.1 Surface models

3.1.1 Vacancy surfaces models

We considered two kinds of vacancy defects on pristine graphene, i.e., single vacancy (SV) and double vacancy (DV), and three types of stone-wales defects, i.e., Stone-Wales (SW), vacancy Stone-Wales arrangement-1 (VSW-1), and vacancy Stone-Wales arrangement-2 (VSW-2). The optimized structures are shown in Figure 1 and Figure 2. The formation energies of defective graphene with respect to pristine graphene (Figure 1a) are in Table 1, which are in excellent agreement with previous benchmarks.

Simple vacancy defects. SV is the most basic defect in graphene and can be observed using transmission electron (TEM) and scanning tunneling (STM) microscopies.^{15,16} Upon the local Jahn-Teller distortion, there is only one carbon atom with a dangling bond at a distance of 1.395 Å to the closest neighbor, much shorter than in pristine graphene, 1.426 Å (Figure 1b). Ugeda *et al.* found

an increase in the local density of states on SV's dangling bond, triggering a protrusion in the STM images.³⁴ The SV formation energy is 7.64 eV, which is in accordance with the previous literature.³⁵⁻³⁶ The DV is created by removing two neighboring atoms, see Figure 1c. The fully relaxed DV presents no dangling bonds and features two pentagons and one octagon instead of four hexagons in the perfect graphene. The formation energy of a DV is 7.49 eV, also in agreement with benchmark values.^{37,38}

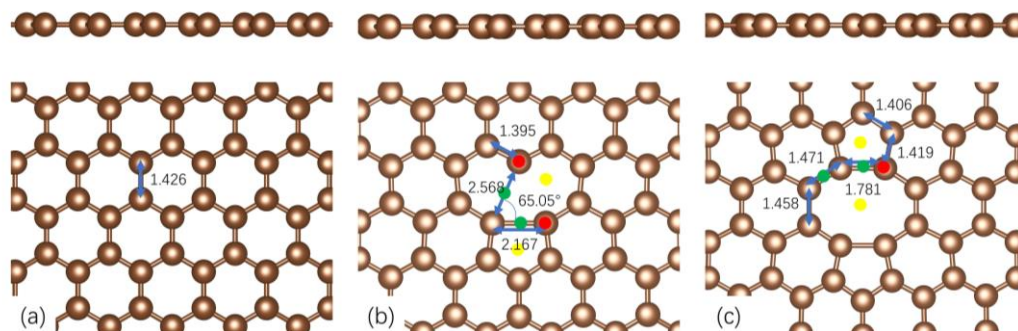


Figure 1. Structure representations of (a) pristine graphene, (b) single vacancy, and (c) double vacancy on graphene. Khaki spheres represent the carbon atoms. Red, yellow, and green dots indicate top, hollow, and bridge adsorption sites. Distances are given in Å.

Stone-Wales defects are generated by reconstructing the graphitic lattice, i.e., switching between pentagons, hexagons, and heptagons. These are regular in carbon material with sp^2 hybridization. As seen in Figure 2a, four hexagons are transformed into two pentagons and two heptagons in the Stone-Wales defect (SW) by rotating one of the C-C bonds by 90° . SW has formation energy of 4.76 eV. The rotation of one bond in the DV's octagon transforms the defect into a vacancy Stone-Wales defect arrangement-1 (VSW-1) with three pentagons and three heptagons, see Figure 2b.²¹ The total formation energy of this defect is 6.15 eV, which is 1.34 eV lower than that of DV, implying a thermodynamically favorable reconstruction. Rotating one more edge C-C bond in the heptagons transforms VSW-1 to VSW-2, see Figure 2c. This defect's formation energy is 7.14 eV, higher than the VSW-1 by 1 eV and in agreement with the former investigations.¹⁸ These last VSW types of defects are frequently observed in electron microscopy experiments.¹⁷ Among these three Stone-Wales defects, the bond rotation only creates the surface fluctuation on SW with the shortest C-C bond.

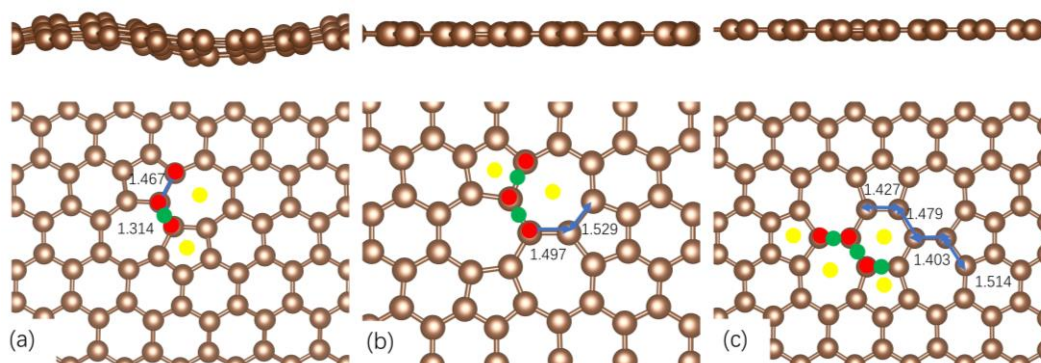


Figure 2. Structure of the reconstructed graphene defects (a) Stone-Wales, (b) vacancy Stone-Wales-1, and (c) vacancy Stone-Wales-2. Khaki spheres represent carbon atoms. Red, yellow, and green dots indicate top, hollow, and bridge adsorption sites. Distances are given in Å.

Table 1. Formation energies of defective graphene structures with respect to pristine graphene.

Surface	This work (eV)	Reference (eV)
SV	7.64	7.78 (LDA), ³⁵ 7.80 (PW91), ³⁹ 7.0±0.5(Exp.) ³⁶
DV	7.49	8.7 (Exp.) ³⁷ , 7.6 (LDA) ³⁸
SW	4.76	5.2 (LDA), ⁴⁰ 4.8 (PW91), ⁴⁰ 4.82 (PBE) ⁴¹
VSW-1	6.15	-
VSW-2	7.14	-

3.1.2 Doped surface models

The charge and spin density distribution of graphene could be modified by dopants, an effective method to tune graphite surfaces' properties.⁴² We considered the substitution of one graphitic (from pristine lattice) or pyridinic carbon (from a vacancy) by a heteroatom, e.g., O, N, B, and S. Besides, we have also included the carboxyl and hydroxyl groups as local defects.

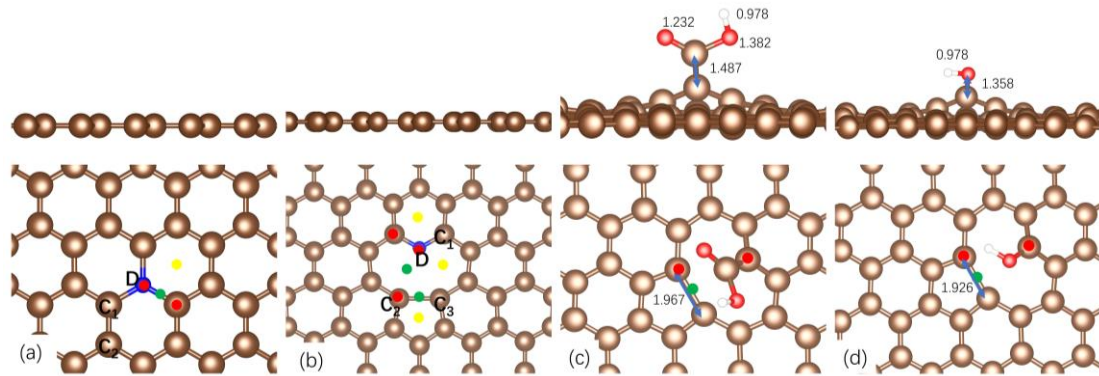


Figure 3. Representation of doped structures: (a) graphitic, (b) pyridinic, (c) carboxyl, and (d) hydroxyl group. The blue and khaki spheres represent the dopant and carbon atoms, respectively. Red, yellow and green buttons represent top, hollow, and bridge sites. In c and d, red and white spheres represent oxygen and hydrogen.

As shown in Table 2, among the graphitic dopant, only graphitic N dopants (GN) shorten the lattice length from 1.426 Å in pristine graphene to 1.415 Å. The pyridinic nitrogen-doped system (PN) presents the closest bond length between the heteroatom and the lattice-carbon atoms (DC₁ label in Figure 3). The graphitic sulfur-doped (GS) structure has the most severe lattice expansion as S has the biggest atomic radius of the dopants considered. Due to the atomic radius's size relative to the carbon atom, PO and PN increase the angles $\angle DC_2C_3$ compared with the angle of 65.1° in SV, while PB and PS decrease it. Especially in PB, with a small atomic radius and electronegativity, the boron atom moves closer to the defect center. The presence of a carboxyl and hydroxyl group pull up the dangling carbon, shortening the C-C distance compared with SV.

Table 2. Structural parameters of graphitic and pyridinic doped graphene structures. Pristine graphene, SV, COOH and OH values are included for the comparison. Labels D, C₁, DC₂, C₃ are depicted in Figure 3.

	Graphitic dopant		Pyridinic dopant			
	DC ₁ (Å)	∠DC ₁ C ₂ (°)	DC ₁ (Å)	DC ₂ (Å)	C ₂ C ₃ (Å)	∠DC ₂ C ₃ (°)
Graphene	1.426	120.0	1.395	-	-	-
SV	-	-	-	2.568	2.167	65.1
O	1.489	117.5	1.370	2.559	1.971	67.4
N	1.415	120.1	1.336	2.545	1.910	68.0
B	1.484	118.7	1.535	2.272	2.565	55.6
S	1.627	116.7	1.634	2.393	2.158	63.2

3.2 NH₃ adsorption and reforming

We have investigated all the non-equivalent adsorptions and configurations of the species along the NH₃ reforming process to derive the relative energies between them as a function of the local surface defects. Table 3 summarizes the adsorption and relative energies of the most favorable configurations of NH_x (x = 1 - 3) and atomic and molecular hydrogen and nitrogen. The adsorption modes on SV and DV are represented in Figure S1 of the supplementary information (SI) and on PO, GO, and PN in Figure S2 as selected doped examples.

Table 3. Molecule adsorption and relative energies of surface species (eV) on the defective graphene surfaces.

Surface	NH ₃ *	NH ₂ *	NH*	N*	H*	N ₂ *	H ₂ *
Pristine	-0.11	2.47	4.29	4.33	1.46	-0.11	-0.07
SV	-1.28	-1.55	-4.07	-6.65	-2.17	-2.31	-2.54
DV	-0.15	-0.63	-2.07	-1.98	0.00	-0.12	-0.03
SW	-0.14	1.21	1.64	2.20	0.40	-0.11	-0.06
VSW-1	-0.10	0.77	2.24	2.98	-0.24	-0.09	-0.04
VSW-2	-0.12	1.12	2.37	2.00	0.22	-0.09	-0.05
GO	-0.02	-0.88	-0.43	0.54	-1.39	0.07	-0.06
PO	-0.11	0.24	-1.78	-1.69	-0.77	0.13	-0.04
GN	-0.67	0.60	2.75	2.96	0.25	-0.67	-0.37
PN	-0.16	-0.26	-1.97	-2.15	-1.08	0.40	-0.01
GB	-0.66	0.61	1.82	2.71	0.13	-0.67	-0.36
PB	-0.97	-1.56	-3.46	-6.57	-1.88	-0.28	-0.21
GS	-0.17	0.20	0.97	1.93	-0.27	-0.09	-0.06
PS	-0.69	-1.05	-2.98	-2.92	-1.47	-2.00	-0.36
COOH	-0.48	0.37	-1.37	-4.19	-0.74	-0.14	-2.77
OH	-0.55	0.58	-1.56	-4.40	-0.61	-0.13	-0.08

According to Sabatier's principle, the optimal interaction of reactive species with the catalysts should be neither too weak nor too strong. Due to the inactive π system in pristine graphene, SW,

VSW-1, VSW-2, GN, GB, and GS (as shown in Figure S3), their interaction with NH_2 and NH are very weak or unfavorable, and hence, these are not considered further for the mechanistic study. On the other hand, the weakening of the conjugated π system in SV, DV, GO, PO, PN, PB, and PS creates the active region for the reactants to interact, making these defects promising candidates to catalyze the ammonia reforming. The low electron density at the pz orbital of dangling carbon connected to COOH and OH is not enough to stabilize the NH_2 upon the first hydrogenation inhibiting the process (Table 3).

SV can adsorb the NH_3 molecule effectively with an N-C distance of 1.475 Å. However, upon NH_3 complete dehydrogenation, the N atom incorporates into the carbon lattice with a rather exothermic step. This process could be used as a method for N-dope graphene materials. The DV interaction with reaction intermediates depends on the number of hydrogens attached to N, which finally is incorporated in the carbon lattice. In the case of doped C-structures, the introduction of oxygen and nitrogen in the lattice rearranges the electronic structure and, since the electronegativity sequence is $\text{O} > \text{N} > \text{C}$ and the ammonia molecule has an unpaired electron, the preferable ammonia adsorption is the nearby unpopulated C-orbitals, i.e., next to the dopant or opposite to the pyridinic heteroatom. The electron density localized at the PO and PN difficulties the adsorption of NH_3 but not the electron-deficient NH_x ($x \leq 2$). Other heteroatoms like B and S in pyridinic positions are reactive and dehydrogenate NH_3 spontaneously, leaving N and H atoms firmly bound to the surface. Interestingly, the presence of COOH and OH species behaves similarly to PB and PS, except that the first dehydrogenation is endothermic.

3.3 Thermochemistry

The calculated energy profiles for NH_3 reforming on local defects, i.e., vacancies and doped graphene surfaces, are shown in Figure 4 and Figure 5. The energy differences of SW, VSW-1, VSW-2, GN, GB, and GS during the dehydrogenation are endothermic, similar to pristine graphene. The only carbon-defective system with a moderate NH_3 reforming pathway is DV ($|\Delta E_{\text{max}}| < 2.07$ eV), which seems a suitable candidate as a non-metallic catalyst.

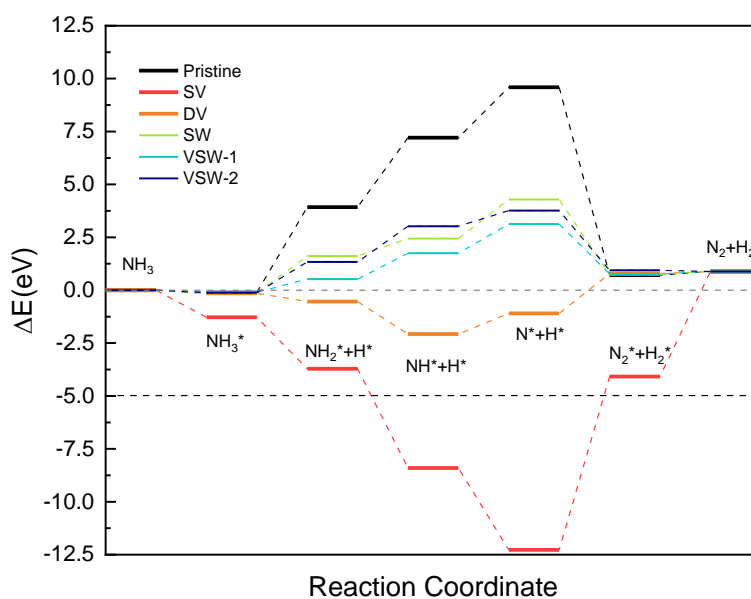


Figure 4. Thermodynamic energy profile of NH₃ reforming on defective graphene. Pristine graphene is also represented for comparison. The asterisk (*) denotes surface species. The dashed line at -5 eV indicates an arbitrary limit set to guide the eye.

The complete NH₃ dehydrogenation is thermodynamically favorable on PN, PB, GO, PO, PS, OH, and COOH surfaces (Figure 5). However, severe surface deformation and high energy differences between elementary steps, e.g., the recombination of N₂ and H₂ on PB, suppress the overall reaction possibility on PB, PS, OH, and COOH. Considering that the reaction energies along the pathway should be moderate, we will investigate every elementary reaction on PO, GO, and PN.

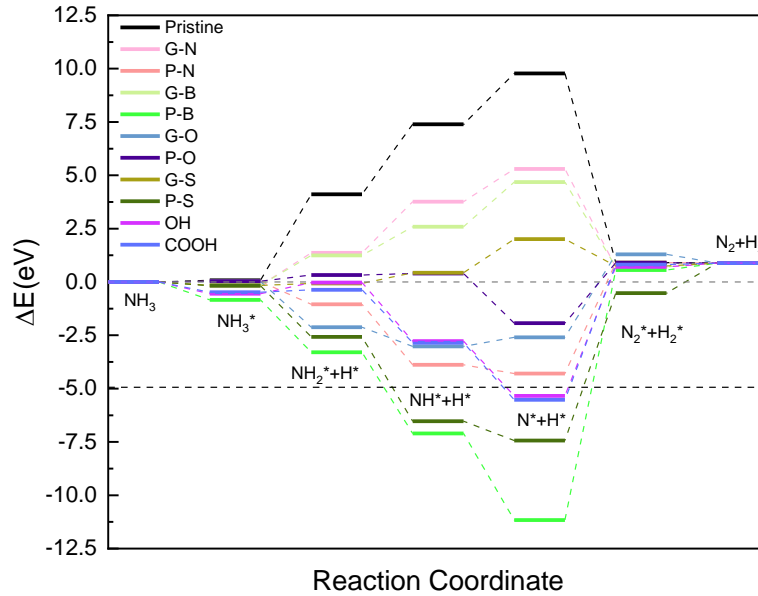


Figure 5. Thermodynamic energy profiles of NH₃ reforming on doped graphene. Pristine graphene is also represented for comparison. The asterisk (*) denotes surface species. The dashed line at -5 eV indicates an arbitrary limit set to guide the eye.

The electron transfer between the N in NH₃ and the C-dangling bonds plays a crucial role in activating the N-H bond required for triggering the first dehydrogenation step. Therefore, SV, DV, PO, GO, and PN surfaces are selected from the defects above for further thermodynamic and kinetic investigations. We computed the free reaction and barrier energies of ammonia reforming according to the reaction mechanism in Table 4. We plotted them as a function of the temperature in Figure 6 and Figure S4, where the ‘R + odd numbers’ are the direct reactions and ‘R + even numbers’ are the reverse reactions, respectively.

Table 4. Elementary steps in ammonia reforming process—asterisk (*) denotes a free surface site and surface species.

No.	Dehydrogenation/recombination	No.	Adsorption/Desorption
R1	$\text{NH}_3^* + * \rightarrow \text{NH}_2^* + \text{H}^*$	A1	$\text{NH}_3 + * \rightarrow \text{NH}_3^*$
R2	$\text{NH}_2^* + \text{H}^* \rightarrow \text{NH}_3^* + *$	D1	$\text{NH}_3^* \rightarrow \text{NH}_3 + *$
R3	$\text{NH}_2^* + * \rightarrow \text{NH}^* + \text{H}^*$	A2	$\text{H}_2 + * \rightarrow \text{H}_2^*$
R4	$\text{NH}^* + \text{H}^* \rightarrow \text{NH}_2^* + *$	D2	$\text{H}_2^* \rightarrow \text{H}_2 + *$

R5	$\text{NH}^* + * \rightarrow \text{N}^* + \text{H}^*$	A3	$\text{N}_2 + * \rightarrow \text{N}_2^*$
R6	$\text{N}^* + \text{H}^* \rightarrow \text{NH}^* + *$	D3	$\text{N}_2^* \rightarrow \text{N}_2 + *$
R7	$2\text{N}^* \rightarrow \text{N}_2^* + *$		
R8	$\text{N}_2^* + * \rightarrow 2\text{N}^*$		
R9	$2\text{H}^* \rightarrow \text{H}_2^* + *$		
R10	$\text{H}_2^* + * \rightarrow 2\text{H}^*$		

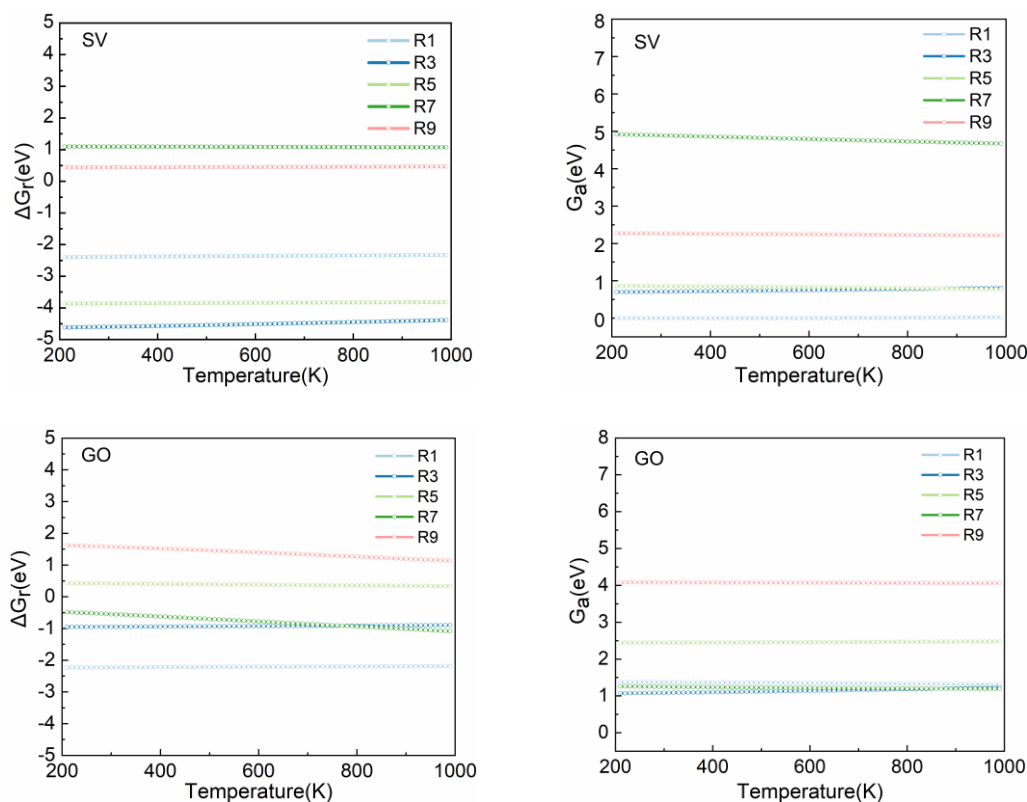


Figure 6. Free reaction (ΔG_r) and barrier (G_a) energies of the elementary steps in the ammonia dehydrogenation (R1, R3, R5) and molecular N_2 and H_2 formations (R7 and R9) on SV and GO as a function of the temperature.

The ammonia's N-H bond activation in R1 represents the molecule's stability on the surfaces and its dehydrogenation likelihood. Hence, the high active barrier of R1 on DV, PO and PN inhibits the dehydrogenation process. Further investigations on the use of synergistic carbon-catalyst may help overtake the first NH_3 dehydrogenation (on DV and PN) or facilitate the H_2 desorption, explaining the improvement of activity in the oxidative coupling of amines to imines when creating defects over graphene.¹² Compared with defective graphene, H adatoms associative recombination (R9) is the rate-determining step on the three doped surfaces (PO, GO, and PN). It has a significant activation energy (~ 4 eV) and is highly endothermic. Therefore, PO, GO, and PN catalysts will be deactivated quickly by hydrogen poisoning.

3.4 Microkinetics

Every elementary step's reaction rate constants were calculated based on the DFT outcomes and summarized in Table S1 and S2 in the SI.

3.4.1 Temperature programmed desorption (TPD)

We simulated the individual desorption of N₂ and H₂ from the considered surfaces as a crucial step to complete the catalytic cycle. Figure 7 shows that the N₂ molecule cannot desorb easily from SV and DV due to the strong interaction between the N atom and the carbon's dangling bond, *i.e.*, the N atom fills the C-vacancy, decreasing the surface's free energy dramatically (Figure 4). On the other hand, N₂ desorption from GO and PO occurs at accessible although very different temperatures (400 K and 640 K at 0.15 ML, respectively) again due to the N's strong interaction with C-dangling bonds. Such interaction is weaker in PN's presence because of the electronic structure difference between N (one lone pair of electrons) and O atom (two lone pair of electrons). Since the dopant (O, N) participates in the conjugated π system, the interaction between H and C-dangling bonds on the dopant system is more favorable than on vacancy surfaces. The desorption temperature of H₂ is mild (460 K at 0.15 ML) on DV because of the recovery of the pentagon structure after the desorption. As seen in the thermochemistry section, H₂ evolution from PN, PO, and GO is very unfavorable and occurs at temperatures higher than 1000K. Generally, with the rise of N and H coverage on the investigated surfaces, the TPD patterns of both molecules have a ~ 25 K shift to lower temperatures.

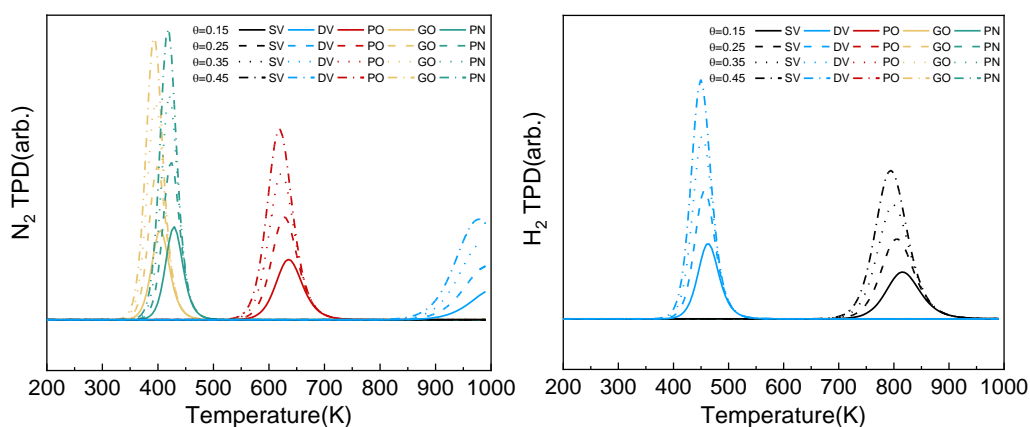


Figure 7. Simulated N₂ (left) and H₂ (right) TPD patterns on different graphene local defects at various initial coverages (θ in ML) and with a heating rate of 1 K/min.

3.4.2 Batch reactor simulations

Batch reactor simulations were employed to analyze the NH₃ reforming process on the selected surfaces. Considering the high barrier energy of NH₃ dehydrogenation on DV, PO, and PN, these surfaces will present negligible changes in NH₃ concentration in batch reactor simulations. Contrarily, SV and GO structures showed considerable intake of molecular NH₃ depending on the temperature and exposure time, Figure S11. The NH₃ contents on SV and GO reached the steady-state after ~ 600 s, Figure 8 and Figure 9 respectively.

In terms of SV, the small energy barrier (0.11 eV) of the first dehydrogenation (R1) leads to NH₂ and H adsorbed on the surface. From 300 K, the consecutive dehydrogenation of NH_x species leads to a rapid increase of N and H coverages. As the temperature rises, NH_x and H adatoms recombine, forming NH₃^{*}, which desorbs from the surface establishing an equilibrium between $NH_3 \rightleftharpoons NH_x^* + (3-x)H^*$. Beyond 700 K, the equilibrium is shifted as H₂ desorbs from the active sites. At this stage, N adatoms accumulate on the surfaces breaking the former plateau of ~ 0.25 ML. These results

also revealed the crucial role of high temperature in the synthesis of N-doping graphene/graphite by thermal treatment with NH_3 .^{43,44}

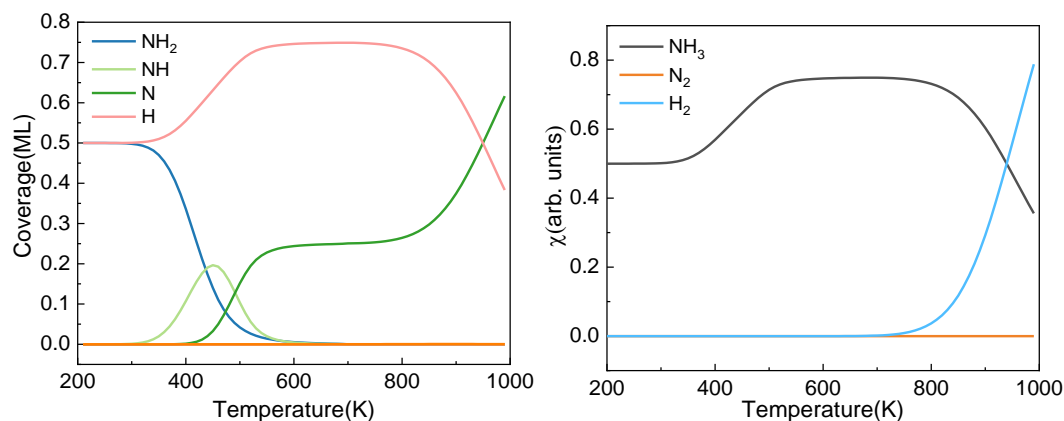


Figure 8. The steady-state of surface species distribution (left) on SV surface and the ratio (χ) of gaseous species (right) as functions of temperature in the batch reactor simulations. The initial ratio of NH_3 : surface sites is 1:1, and the reaction time is 600s.

Opposite to R1 on SV, the NH_3 dehydrogenation requires a temperature as high as 700 K on GO to proceed. R1 is driven by the desorption of N_2 but inhibited by an increase in H coverage, which eventually poisons the active sites. Note that the limited H_2 evolution opens the scope for designing high-Faraday efficient electrocatalysts based on GO structures. Contrary to carbon vacancies, the GO structure is not favorable as a precursor for the synthesis of N-doping graphene/graphite as confirmed in previous research.^{45,46}

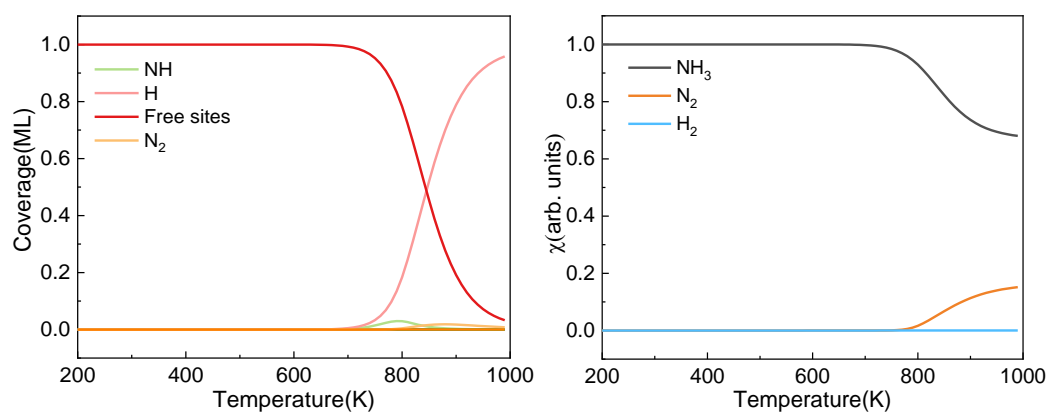


Figure 9. The steady-state of surface species distribution (left) on GO surface and the ratio (χ) of gaseous species (right) as functions of temperature in the batch reactor simulations. The initial ratio of NH_3 : surface sites is 1:1, and the reaction time is 600s.

3.5 Why do SV defects activate NH_3 molecules?

We analyzed the electronic structure of the isolated and NH_3 -adsorbed systems using the density of states (DOS) and the Bader atoms-in-molecule methods to characterize SV's N-C interaction. Bader

analysis showed that a charge transfer of $0.37 e^-$ from NH_3 to the SV surface site upon adsorption drives a charge depletion from all the N-H bonds ($0.34 e^-$), weakening it and promoting its scission in agreement with the mentioned bond elongation results (Figure 10(a)). Moreover, the DOS projection on the H orbitals (Figure 10(b)) shows the electronic structure rearrangement upon NH_3 adsorption on the SV site. The increase in H-states above the Fermi energy further indicates the activation of N-H bond.

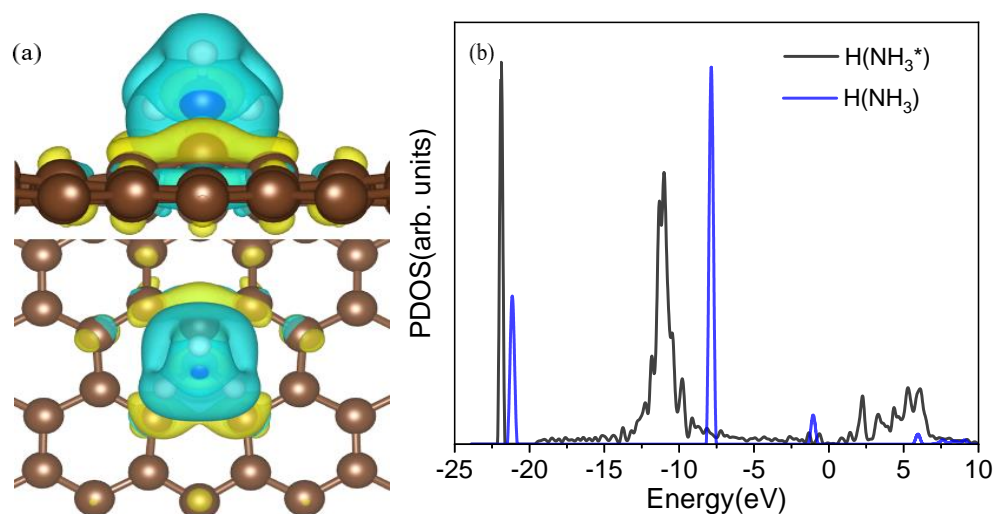


Figure 10. (a) Partial charge density flow upon NH_3 adsorption (top view and side view). Yellow and blue iso-surfaces denote gain and depletion of electron density with an iso-surface value of $0.01 e/\text{\AA}^3$. The blue sphere represents N; white is H, and khaki is C. (b) DOS diagram of isolate and adsorbate NH_3 on SV projected on the hydrogen atoms in the molecule.

4 Conclusions

The catalytic activity of carbon materials was investigated by analyzing the NH_3 reforming mechanism on pristine and a series of point defects graphene (C-vacancy and dopants). We modeled the surfaces and compared our results with previous benchmarks. We explored the different adsorption sites and conformation of the species involved in the NH_3 reforming, i.e., NH_x ($x = 1-3$), H and N, and H_2 and N_2 . We identified that vacancies (SV and DV) and doped (PN, PO, and GO) structures to be potential catalysts by comparing the thermodynamic reaction pathways. We found the reforming rate-determining steps to be the NH_3 activation and first dehydrogenation and the N and H recombination and molecular desorption. These results imply that co-catalysts may be able to accelerate and tune the graphite catalytic activity, e.g., for high-efficient electrocatalysts. Batch reaction simulations described the reaction processes along the temperature and time. They indicated that although SV and GO can dehydrogenate NH_3 , these sites will be poisoned respectively by N and H adatoms' strong interactions. We rationalized the NH_3 activation on carbon dangling bonds based on electronic analysis, which indicated a charge transfer of $0.37 e^-$ from the N-H bond to the SV, triggering the NH_3 first dehydrogenation. The study demonstrated that the carbon-based materials are long-term inert supports for the catalytic NH_3 reforming even in the presence of defects.

Supporting Information

Additional information is provided in a separate section containing a more detailed discussion of the adsorption structures, the pz orbital partial charge distribution and the methodology related to microkinetic calculations.

Author Information

Corresponding Authors: Alberto Roldan - Cardiff Catalysis Institute, School of Chemistry, Cardiff University, Main Building, Park Place, Cardiff, CF10 3AT, UK; E-mail: RoldanMartinezA@cardiff.ac.uk

Author: Xiuyuan Lu - Cardiff Catalysis Institute, School of Chemistry, Cardiff University, Main Building, Park Place, Cardiff, CF10 3AT, UK.

Acknowledgment

X. Lu acknowledges the China Scholarship Council and Cardiff University for the overseas student scholarship (CSC No. 201806370221). Via membership of the UK's HPC Materials Chemistry Consortium, which is funded by EPSRC (EP/L000202, EP/R029431), this work used the UK Materials and Molecular Modelling Hub for computational resources, MMM Hub, which is partially funded by EPSRC (EP/T022213/1). We also acknowledge computing time on the facilities at Cardiff University managed by the Advanced Research Computing @ Cardiff (ARCCA). All data created during this research are openly available from the University of Cardiff Research Portal orca websites under the DOI: 10.17035/d.2021.0133323569.

Reference

- (1) Abe, J. O.; Popoola, A. P. I.; Ajenifuja, E.; Popoola, O. M. Hydrogen Energy, Economy and Storage: Review and Recommendation. *International Journal of Hydrogen Energy* **2019**, *44* (29), 15072–15086.
- (2) Dincer, I.; Acar, C. Review and Evaluation of Hydrogen Production Methods for Better Sustainability. *International journal of hydrogen energy* **2015**, *40* (34), 11094–11111.
- (3) Bell, T.E.; Ménard, H.; Carballo, J.M.G.; Tooze, R.; Torrente-Murciano, L. Hydrogen production from ammonia decomposition using Co/ γ -Al₂O₃ catalysts—Insights into the effect of synthetic method. *International Journal of Hydrogen Energy* **2020**, *45* (51), 27210–27220.
- (4) Bell, T. E.; Torrente-Murciano, L. H₂ Production via Ammonia Decomposition Using Non-Noble Metal Catalysts: A Review. *Topics in Catalysis* **2016**, *59* (15–16), 1438–1457.
- (5) Mah, A. X. Y.; Ho, W. S.; Bong, C. P. C.; Hassim, M. H.; Liew, P. Y.; Asli, U. A.; Kamaruddin, M. J.; Chemmangattuvalappil, N. G. Review of Hydrogen Economy in Malaysia and Its Way Forward. *International Journal of Hydrogen Energy* **2019**, *44* (12), 5661–5675.
- (6) Lamb, K. E.; Dolan, M. D.; Kennedy, D. F. Ammonia for Hydrogen Storage: A Review of Catalytic Ammonia Decomposition and Hydrogen Separation and Purification. *International Journal of Hydrogen Energy* **2019**, *44* (7), 3580–3593.
- (7) Smith, C.; Hill, A. K.; Torrente-Murciano, L. Current and Future Role of Haber–Bosch Ammonia in a Carbon-Free Energy Landscape. *Energy & Environmental Science* **2020**, *13* (2), 331–344.
- (8) Yürüm, Y.; Taralp, A.; Veziroglu, T. N. Storage of Hydrogen in Nanostructured Carbon Materials. *International journal of hydrogen energy* **2009**, *34* (9), 3784–3798.

- (9) Pereira, M. F. R.; Figueiredo, J. L.; Órfão, J. J.; Serp, P.; Kalck, P.; Kihn, Y. Catalytic Activity of Carbon Nanotubes in the Oxidative Dehydrogenation of Ethylbenzene. *Carbon* **2004**, *42* (14), 2807–2813.
- (10) Qu, L.; Liu, Y.; Baek, J.-B.; Dai, L. Nitrogen-Doped Graphene as Efficient Metal-Free Electrocatalyst for Oxygen Reduction in Fuel Cells. *ACS nano* **2010**, *4* (3), 1321–1326.
- (11) Zhang, L.; Xu, Q.; Niu, J.; Xia, Z. Role of Lattice Defects in Catalytic Activities of Graphene Clusters for Fuel Cells. *Physical Chemistry Chemical Physics* **2015**, *17*(26), 16733–16743.
- (12) Su, C.; Acik, M.; Takai, K.; Lu, J.; Hao, S.; Zheng, Y.; Wu, P.; Bao, Q.; Enoki, T.; Chabal, Y. J. Probing the Catalytic Activity of Porous Graphene Oxide and the Origin of This Behaviour. *Nature communications* **2012**, *3*(1), 1–9.
- (13) Navalon, S.; Dhakshinamoorthy, A.; Alvaro, M.; Garcia, H. Carbocatalysis by Graphene-Based Materials. *Chemical reviews* **2014**, *114* (12), 6179–6212.
- (14) Su, D. S.; Perathoner, S.; Centi, G. Nanocarbons for the Development of Advanced Catalysts. *Chemical reviews* **2013**, *113* (8), 5782–5816.
- (15) Anton, R.; Schneidereit, I. In Situ TEM Investigations of Dendritic Growth of Au Particles on HOPG. *Physical Review B* **1998**, *58* (20), 13874.
- (16) Rodríguez-Manzo, J. A.; Cretu, O.; Banhart, F. Trapping of Metal Atoms in Vacancies of Carbon Nanotubes and Graphene. *ACS nano* **2010**, *4* (6), 3422–3428.
- (17) Lee, G.-D.; Wang, C. Z.; Yoon, E.; Hwang, N.-M.; Kim, D.-Y.; Ho, K. M. Diffusion, Coalescence, and Reconstruction of Vacancy Defects in Graphene Layers. *Physical review letters* **2005**, *95* (20), 205501.
- (18) Banhart, F.; Kotakoski, J.; Krasheninnikov, A. V. Structural Defects in Graphene. *ACS nano* **2011**, *5* (1), 26–41.
- (19) Yadav, S.; Zhu, Z.; Singh, C. V. Defect Engineering of Graphene for Effective Hydrogen Storage. *International journal of hydrogen energy* **2014**, *39* (10), 4981–4995.
- (20) Kresse, G.; Furthmüller, J. Efficiency of Ab-Initio Total Energy Calculations for Metals and Semiconductors Using a Plane-Wave Basis Set. *Computational materials science* **1996**, *6* (1), 15–50.
- (21) Bucko, T.; Hafner, J.; Lebegue, S.; Angyán, J. G. Improved Description of the Structure of Molecular and Layered Crystals: Ab Initio DFT Calculations with van Der Waals Corrections. *The Journal of Physical Chemistry A* **2010**, *114* (43), 11814–11824.
- (22) Hammer, B.; Hansen, L. B.; Nørskov, J. K. Improved Adsorption Energetics within Density-Functional Theory Using Revised Perdew-Burke-Ernzerhof Functionals. *Physical review B* **1999**, *59* (11), 7413.
- (23) Perdew, J. P.; Burke, K.; Ernzerhof, M. Generalized Gradient Approximation Made Simple. *Physical review letters* **1996**, *77* (18), 3865.
- (24) Kresse, G.; Joubert, D. From Ultrasoft Pseudopotentials to the Projector Augmented-Wave Method. *Physical review b* **1999**, *59* (3), 1758.
- (25) Blöchl, P. E.; Jepsen, O.; Andersen, O. K. Improved Tetrahedron Method for Brillouin-Zone Integrations. *Physical Review B* **1994**, *49* (23), 16223.
- (26) Grimme, S.; Ehrlich, S.; Goerigk, L. Effect of the Damping Function in Dispersion Corrected Density Functional Theory. *Journal of computational chemistry* **2011**, *32* (7), 1456–1465.
- (27) Geim, A. K. Graphene: Status and Prospects. *science* **2009**, *324* (5934), 1530–1534.

- (28) Sheppard, D.; Xiao, P.; Chemelewski, W.; Johnson, D. D.; Henkelman, G. A Generalized Solid-State Nudged Elastic Band Method. *The Journal of chemical physics* **2012**, *136* (7), 074103.
- (29) Ghasemi, A.; Xiao, P.; Gao, W. Nudged Elastic Band Method for Solid-Solid Transition under Finite Deformation. *The Journal of Chemical Physics* **2019**, *151* (5), 054110.
- (30) Xiao, P.; Sheppard, D.; Rogal, J.; Henkelman, G. Solid-State Dimer Method for Calculating Solid-Solid Phase Transitions. *The Journal of Chemical Physics* **2014**, *140* (17), 174104.
- (31) Evans, M. G.; Polanyi, M. Some Applications of the Transition State Method to the Calculation of Reaction Velocities, Especially in Solution. *Transactions of the Faraday Society* **1935**, *31*, 875–894.
- (32) Eyring, H. The Activated Complex and the Absolute Rate of Chemical Reactions. *Chemical Reviews* **1935**, *17* (1), 65–77.
- (33) Eyring, H. The Activated Complex in Chemical Reactions. *The Journal of Chemical Physics* **1935**, *3* (2), 107–115.
- (34) Ugeda, M. M.; Brihuega, I.; Guinea, F.; Gómez-Rodríguez, J. M. Missing Atom as a Source of Carbon Magnetism. *Physical Review Letters* **2010**, *104* (9), 096804.
- (35) Wang, Z.; Zhou, Y. G.; Bang, J.; Prange, M. P.; Zhang, S. B.; Gao, F. Modification of Defect Structures in Graphene by Electron Irradiation: Ab Initio Molecular Dynamics Simulations. *The Journal of Physical Chemistry C* **2012**, *116* (30), 16070–16079.
- (36) Thrower, P. A.; Mayer, R. M. Point Defects and Self-Diffusion in Graphite. *Physica Status Solidi. A, Applied Research* **1978**, *47* (1), 11–37.
- (37) El-Barbary, A. A.; Telling, R. H.; Ewels, C. P.; Heggie, M. I.; Briddon, P. R. Structure and Energetics of the Vacancy in Graphite. *Physical Review B* **2003**, *68* (14), 144107.
- (38) Kaxiras, E.; Pandey, K. C. Energetics of Defects and Diffusion Mechanisms in Graphite. *Physical review letters* **1988**, *61* (23), 2693.
- (39) Singh, R.; Kroll, P. Magnetism in Graphene Due to Single-Atom Defects: Dependence on the Concentration and Packing Geometry of Defects. *Journal of Physics: Condensed Matter* **2009**, *21* (19), 196002.
- (40) Li, L.; Reich, S.; Robertson, J. Defect Energies of Graphite: Density-Functional Calculations. *Physical Review B* **2005**, *72* (18), 184109.
- (41) Ma, J.; Alfe, D.; Michaelides, A.; Wang, E. Stone-Wales Defects in Graphene and Other Planar sp^2 -Bonded Materials. *Physical Review B* **2009**, *80* (3), 033407.
- (42) Wang, H.; Maiyalagan, T.; Wang, X. Review on Recent Progress in Nitrogen-Doped Graphene: Synthesis, Characterization, and Its Potential Applications. *ACS Catalysis* **2012**, *2* (5), 781–794.
- (43) Wang, X.; Li, X.; Zhang, L.; Yoon, Y.; Weber, P. K.; Wang, H.; Guo, J.; Dai, H. N-Doping of Graphene through Electrothermal Reactions with Ammonia. *Science* **2009**, *324* (5928), 768–771.
- (44) Lin, Y.-C.; Lin, C.-Y.; Chiu, P.-W. Controllable Graphene N-Doping with Ammonia Plasma. *Applied Physics Letters* **2010**, *96* (13), 133110.
- (45) Li, X.; Wang, H.; Robinson, J. T.; Sanchez, H.; Diankov, G.; Dai, H. Simultaneous Nitrogen Doping and Reduction of Graphene Oxide. *Journal of the American Chemical Society* **2009**, *131* (43), 15939–15944.

- (46) Geng, D.; Chen, Y.; Chen, Y.; Li, Y.; Li, R.; Sun, X.; Ye, S.; Knights, S. High Oxygen-Reduction Activity and Durability of Nitrogen-Doped Graphene. *Energy & Environmental Science* **2011**, 4 (3), 760–764.

TOC:

